Dalton Transactions

ROYAL SOCIETY OF CHEMISTRY

PAPER

View Article Online
View Journal | View Issue

Cite this: *Dalton Trans.*, 2023, **52**, 8262

Thermally processed Ni-and Co-struvites as functional materials for proton conductivity†

Stephanos Karafiludis,*[a,b] Biswajit Bhattacharya,[a] Ana Guilherme Buzanich,[a] Friedrich Fink,[a] Ines Feldmann,[a] Johan E. ten Elshof,[c] Franziska Emmerling[a,b] and Tomasz M. Stawski*[a]

Here, we describe how to synthesise proton-conductive transition metal phosphates (TMPs) by direct thermal processing of precursor M-struvites, $NH_4MPO_4{\cdot}6H_2O$, with M = Ni^{2+}, Co^{2+}. In the as-derived TMP phases their thermal history and bulk proton conductivity were linked with the structural information about the metal coordination, phosphate groups, and volatile compounds. These aspects were investigated with vibrational and synchrotron-based spectroscopic methods (FT-IR, FT-RS, XAS). We elucidated the structures of amorphous and crystalline Ni- and Co phosphate phases in association with different coordination changes and distortion degrees of the metal polyhedra as they developed upon heating. Ni-struvite transformed to a stable amorphous phase over a broad range of temperatures (90 °C < T < 600 °C), in which it remained in an octahedral coordination environment, but the degree of distortion changed with T. In contrast, heating of Co-struvite led to several successive crystalline phases with only unstable transitional and short-lived amorphous components. Among the as-occurring phases, a highly functional layered M-dittmarite $NH_4MPO_4{\cdot}H_2O$ obtained at low temperatures (T < 200 °C) demonstrated high proton conductivity values of 4.2×10^{-5} S cm^{-1} for Ni-dittmarite and Co-dittmarite > 10^{-4} S cm^{-1} at room temperature. Even at low humidity, these values are comparable with those found for Nafion, MOFs, some perovskites or composite materials. Coprecipitation of phosphates and transition metal cations in the form of struvite is potentially a viable method to extract these elements from wastewater. Thus, we propose that recycled M-struvites could be potentially further directly upcycled into crystalline and amorphous TMPs useful for electrochemical applications.

Received 20th March 2023,
Accepted 25th May 2023

DOI: 10.1039/d3dt00839h

rsc.li/dalton

Introduction

Transition metal phosphates (TMPs) have attracted considerable attention due to their favourable properties for electro-, photo- or organic catalysis and proton exchange membranes.[1–7] For example, TMPs are known as cost-effective cathode materials in lithium/sodium battery technologies,[8–11] for their adequate catalytical performance in the oxygen evolution reaction[12–14] or in organic reactions[15–17] such as the selective oxidation of methane.[18]

TMPs are highly suitable for this broad range of applications due to their ability to form thermally stable diverse crystalline and amorphous structures, including transition metals at various oxidation states and in several coordination environments. Each of these structures can exhibit beneficial properties for specific applications. For instance, the distorted phosphate tetrahedrons in TMPs promote the adsorption or incorporation of water molecules,[19,20] advantageous for proton conductivity. TMPs are known to exhibit relatively high proton conductivity of the order of >10^{-2}–10^{-8} S cm^{-1} from 25 °C to temperatures as high as 400 °C.[21–24] For instance, Zr- and Sn-phosphates demonstrate a broad range of applications due to their sufficiently high proton conductivities at ambient conditions and high temperature.[22,25–27]

Importantly for mass applications, phosphates are readily inexpensive compounds providing potentially high mechanical strength,[28] high thermal stability of the associated stable hydrogen-bonded network, and chemical compatibility with fuel cell device components (electrodes, catalysts, seals, *etc.*).

[a]*Federal Institute for Materials Research and, Testing, Unter den Eichen 87, 12205 Berlin, Germany. E-mail: tomasz.stawski@bam.de, stephanos.karafiludis@bam.de*
[b]*Department of Chemistry, Humboldt-Universität zu Berlin, Brook-Taylor-Straße 2, 12489 Berlin, Germany*
[c]*MESA+ Institute for Nanotechnology, University of Twente, P.O. Box 217, 7500 AE Enschede, the Netherlands*

†Electronic supplementary information (ESI) available: X-ray diffraction (XRD), scanning electron microscopy (SEM), infrared spectroscopy (IR), Raman spectroscopy (RS), thermal gravimetric analysis with differential scanning calorimetry (TGA/DSC), X-ray absorption spectroscopy (XAS), proton conductivity (PC) and dynamic vapor sorption (DVS) measurements, Figs. S1–S12; Tables S1–S23. See DOI: https://doi.org/10.1039/d3dt00839h

In addition, TMPs with tuneable mesoporous frameworks can be synthesized either by using template-based[3,14,20] or template-free methods.[29] Thus, these materials can be obtained in many form factors such as bulk ceramics, thin films, or membrane materials.[30–32] Due to the different condensation degrees of the phosphate units and variable exchangeable metal cations, TMPs provide a wide range of chemical compositions.

Moreover, TMPs can be made through a variety of synthesis procedures such as hydrothermal, mechanochemical, molten salt, or precipitation routes, resulting in highly crystalline to purely amorphous materials, depending on specific requirements.[19,20] Even for near-identical chemical composition, crystalline and amorphous compounds could exhibit completely different physicochemical properties such as solubility, conductivity, or adsorption.[33,34] Nevertheless, due to the lack of long-range order, the structure–property relationships in amorphous solid phases of TMPs are still relatively poorly explored in contrast to their crystalline counterparts.

The necessary challenge in the research on the applicational use of TMPs in all their varieties is an ability to obtain, elucidate and optimise different compositions and structures. This goal can be achieved by processing a universal TMP precursor with a single yet flexible crystal structure. Such potential TMP compound is M-struvite $NH_4MPO_4{\cdot}6H_2O$, where M^{2+} is usually Mg^{2+}, but other divalent cations such as Ni^{2+}, Co^{2+}, Zn^{2+}, Cu^{2+} readily substitute Mg^{2+} in the struvite structure due to similar ionic radii.[35–38] In this work, we focus on Ni- and Co-containing phosphate materials as these are the most promising for electrochemistry.[3,14,39] In our previous study, we showed how to precipitate Co- and Ni-struvites of various morphologies and sizes from aqueous solutions at concentrations similar to those found in wastewaters.[40] Building on this previous work, we present how these recycled M-struvite materials could be potentially further upcycled for electrochemical applications by undergoing a direct thermal treatment (Fig. 1). Consequently, to upcycle and modify these materials for electrochemical applications, a complete understanding of the phase transition sequence during thermal heating and resolving of the complex structures is required. Amorphous and crystalline phases are formed upon the thermal decomposition of Ni- and Co-struvites. We show that some of such as-derived from M-struvite phases, namely M-dittmarites, exhibit high proton conductivity.

Synthesis

$(NH_4)_2HPO_4$ (DAP) (ChemSolute, 99%), $NiSO_4{\cdot}6H_2O$ (ChemSolute, 99%) and $CoSO_4{\cdot}7H_2O$ (Alfa Aesar, 98%) were used to synthesise precursor M-struvites (M = Ni or Co). A detailed description of the synthesis of the precursor transition metal struvites can be found elsewhere.[40] For further analysis, the precursor M-struvites were thermally treated in a temperature series (T-series = 25 °C, 90 °C, 120 °C, 150 °C, 180 °C, 210 °C, 240 °C, 270 °C, 300 °C, 400 °C, 500 °C, 600 °C, 700 °C and 800 °C) with a constant dwell time of t = 24 h to evaluate the thermal decomposition products and related crystalline or amorphous phase transitions. The long dwell time was used to assure equilibration. The following abbreviations are used for the occurring phases: nickel struvite $NH_4NiPO_4{\cdot}H_2O$ (NIS), amorphous phase (am), nickel pyrophosphate $Ni_2P_2O_7$ (NPY), cobalt struvite $NH_4CoPO_4{\cdot}6H_2O$ (COS), cobalt dittmarite $NH_4CoPO_4{\cdot}H_2O$ (COD), hydrogen cobalt(II)

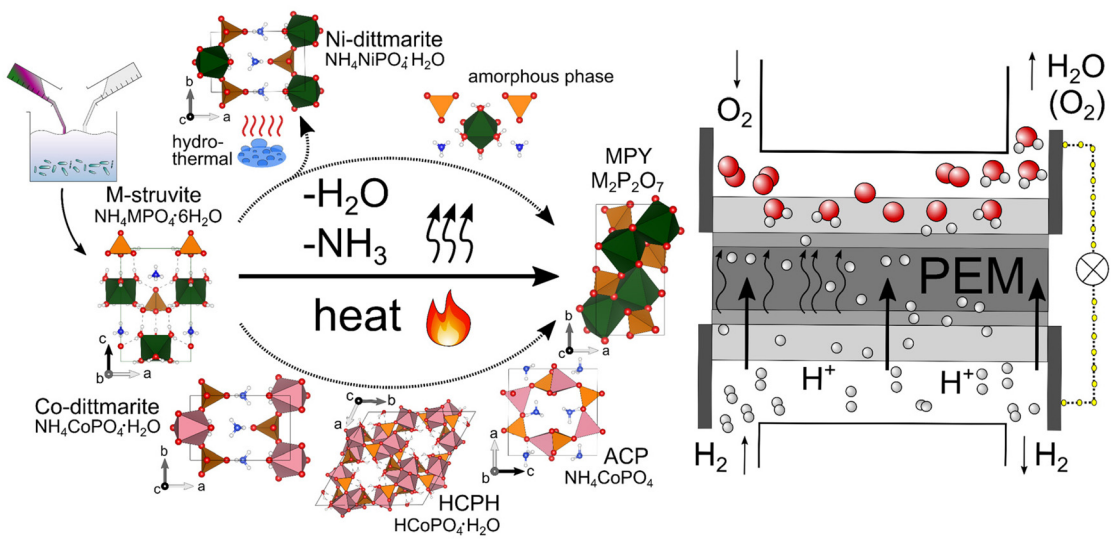

Fig. 1 The precursor M-struvites are obtained by a simple one-pot synthesis and further thermally treated, which results in degassing of H_2O + NH_3 and the associated occurrence of many phases, *e.g.* Ni- and Co-dittmarite, amorphous phases, HCPH, ACP and finally $M_2P_2O_7$ (MPY) with M = Ni, Co. Arrows indicate thermal history, lower arrow (Ni), upper arrow (Co). The synthesis leads to TMP materials potentially suitable for proton exchange membranes (PEMs) in fuel cells. A balance between high thermal stability and significant proton conductivity is the key to their promising applicational use.

phosphate monohydrate $HCoPO_4{\cdot}H_2O$ (HCPH), ammonium cobalt phosphate NH_4CoPO_4 (ACP), cobalt pyrophosphate $Co_2P_2O_7$ (CPY) or M-pyrophospahte (MPY) with M = Ni or Co.

$$NH_4MPO_4 \cdot 6H_2O_{(s)} \rightarrow 0.5\ M_2P_2O_{7(s)} + NH_{3(g)} + 6.5H_2O_{(g)} \quad (1)$$

Upon the heat treatment, M-struvites converted sequentially to amorphous and crystalline phases through many phase transitions on a pathway to a final crystalline M-pyrophosphate, which formed at high temperatures, >500 °C.

The thermal treatment of Co-struvite resulted in the formation of a crystalline Co-dittmarite phase, while Ni-struvite converted completely to an amorphous phase. The Ni-dittmarite analogue was not found directly in the heating experiments. Therefore, in an additional series of experiments, the ~5 g of Ni-struvite precursor powder was put into a hydrothermal autoclave reactor with a small amount of water (<50 ml) and heated up to T = 90 °C to obtain directly crystalline Ni-dittmarite, allowing for a comparison of its properties with those of Co-dittmarite.

Complete technical descriptions of the used characterisation methods, including X-ray diffraction (XRD) for identification of the phase composition, scanning electron microscopy (SEM), combined thermogravimetric analysis, and differential scanning calorimetry (TGA/DSC) for imaging and tracking phase transitions, infrared spectroscopy (IR), Raman spectroscopy (RS), X-ray absorption spectroscopy (XAS) for determination of the coordination environment, proton conductivity (PC) and dynamic vapour sorption (DVS) measurements for evaluation of the applicational use can be found in the ESI (Methods†).

Results and discussion

Composition and morphology of crystalline and amorphous phases

For a clear presentation of the occurring complex phase transitions, we summarise the most important aspects of our synthesis and phases in Fig. 1. Highly crystalline, phase-pure, transition metal M-struvite powders with M = Ni and Co were obtained as precursor materials through a simple one-pot synthesis (Fig. 1),[40] as was evidenced by the X-ray diffraction (Fig. 2A–C).

After treating the precursor Ni- and Co-struvites at different temperatures (T = 90–800 °C, T-series) in air with a dwell time of t = 24 h, chemical and phase composition changes occurred and involved transformations to amorphous and crystalline compounds. The changes were also associated with colour changes of the powders. In the T-series of Ni-struvite, the crystal decomposed to an amorphous phase already at 90 °C (Fig. 2A). Simultaneously, the colour turned from an emerald green (Ni-struvite precursor) to yellow-green at 90 °C to brown at 120 °C. Up to 600 °C, the amorphous phase remained stable. At temperatures >600 °C $Ni_2P_2O_7$ began to crystallise, accompanied by a colour change of the powders from brown to pure yellow (Fig. 2A).

In contrast to Ni-struvite, Co-struvite $NH_4CoPO_4{\cdot}6H_2O$ transformed to crystalline Co-dittmarite $NH_4CoPO_4{\cdot}H_2O$ already after the first heating step at 90 °C (Fig. 2B and C). Up to 210 °C Co-dittmarite remained present until it converted to a mixture of hydrogen cobalt(II)phosphate hydrate $HCoPO_4{\cdot}H_2O$, ammonium cobalt(II)phosphate NH_4CoPO_4, and an amorphous phase (Fig. 1). The amount of NH_4CoPO_4 increased with higher temperatures up to 300 °C while the reflections of $HCoPO_4{\cdot}H_2O$ disappeared. At T = 300 °C, a binary mixture of majorly NH_4CoPO_4 and minorly the amorphous phase(s) was present (Fig. 2B and C). At T = 400 °C $Co_2P_2O_7$ crystallised, although the amorphous phase was still present. Heating to $T \geq 500$ °C, resulted in higher intensities of peaks in the diffractogram. At the same time, the proportion of the amorphous phase decreased successively, meaning that the crystalline phase evolved at the expense of the amorphous component.

Thus, Ni- and Co-struvite systems differ significantly in their thermal decomposition behaviour (Fig. 1). The TGA/DSC analysis was carried out to elucidate the mentioned thermally induced phase transitions, and SE images of the heated samples were collected (ESI: Fig. S2–S4†). A detailed description of the TGA/DSC data can be found in the ESI (Supplementary Data Analysis 1 and Fig. S4†). The thermally induced phase transitions and resulting mass losses due to degassing of volatile compounds are in agreement with the phases detected by XRD measurements. Based on the mass losses and DSC signals, the range of possible chemical compositions of the amorphous phase at given temperatures could be significantly narrowed down (ESI: Supplementary Data Analysis 1†).

The SE images show the presence of a "relict" Ni-struvite crystal morphology in the thermally treated amorphous Ni samples, overall indicating a gradual crystalline-amorphous phase transition and an associated pseudomorphism of the amorphous phases after the crystalline Ni-struvite (Fig. 2D and ESI: Fig. S2†). Even at higher temperatures $T \geq 600$ °C, the relict Ni-struvite morphology can still be observed (Fig. 2D, ESI: Fig. S2†). In this case, the pseudomorphism merely signifies a formation of the amorphous phase(s) without any crystalline intermediate step (Fig. 1A). Crystalline-crystalline pseudomorphism involving usually low volume changes is possible,[41] but is unlikely to occur for these transformations, as the decomposition of M-struvite demonstrates significant volume dilatation due to loss of water and ammonia. Notably, the amorphous inhabited Ni-struvite structure is mechanically weak and can be easily distorted during sample manipulation (ESI: Fig. S2†).

In contrast, the transformation of Co-struvite (Fig. 2E and ESI: Fig. S3†) to other Co-phosphate phases is directly visible as changes in the morphology of the crystals. Here, partial crystalline-crystalline pseudomorphism also occurs *i.e.* of Co-dittmarite after Co-struvite, although the formation of other crystalline phases quickly extinguishes these structures (ESI:

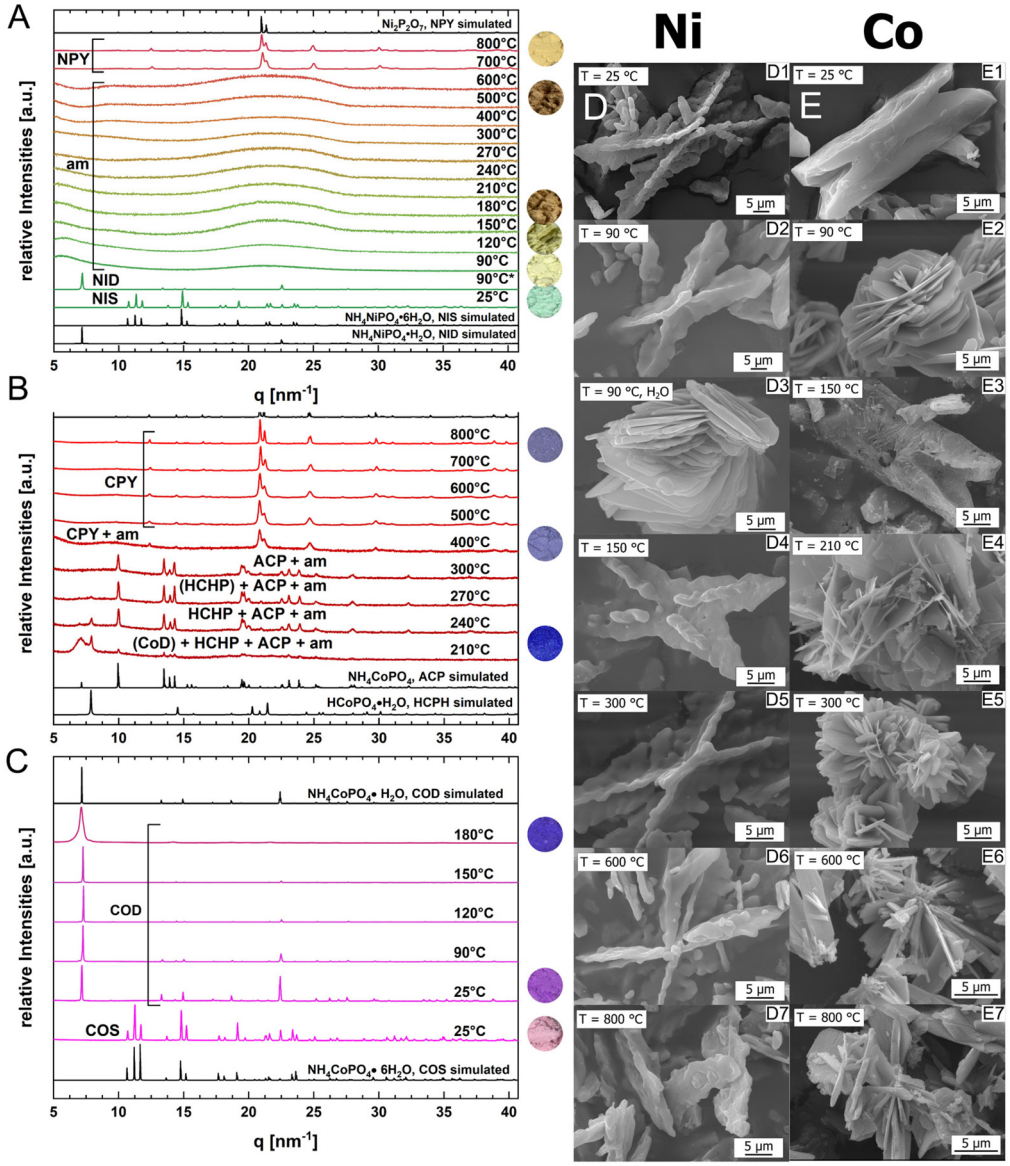

Fig. 2 Diffractograms of *T*-series of (A) Ni- struvite and (B and C) Co-struvite from 25 °C to 800 °C; 90 °C* = hydrothermal synthesis at RH ≈ 100% at 90 °C; simulated XRD patterns were always added at the beginning and end of the diffractogram; The colour of the powder in the circles are placed next to the diagram; selected SE images of (D) Ni- and (E) Co- phosphates heated at different temperatures from 25 to 800 °C. SE images of the complete *T*-series of Ni and Co can be found in the ESI (Fig. S2 and S3†). Ni-struvite (NIS) reference database ICSD 403058; Ni-dittmarite (NID) reference database ICSD 424553; α-$Ni_2P_2O_7$ (NPY) reference ICSD 403058; Co-struvite reference ICSD 170042; Co-dittmarite (COD) with COD reference database 2008122; α -NH_4CoPO_4 (ACP) reference PDF 00-018-0402; Hydrogen cobalt(II)phosphate hydrate (HCPH) reference database ICSD 33828; α -$Co_2P_2O_7$ (CPY) reference database ICSD 280959.

Fig. S3†). At $T > 90$ °C, Co-dittmarite replaces Co-struvite as a pseudomorph at progressing temperatures (Fig. 2E and ESI: Fig. S3†). This is remarkably well-visible as the habit of the former original X-shaped Co-struvite crystals can still be identified (Fig. 2E and ESI: Fig. S3†), although Co-dittmarite covers the whole surface. The crystals' thin 2D sheet morphology indicates a crystalline-crystalline phase transition from Co-dittmarite to mainly HCoPO4·H_2O and NH_4CoPO_4 (Fig. 1, 2E and ESI: Fig. S3†). Above 270 °C, the NH_4CoPO_4 exhibits its final crystal habit as two-dimensional plates similar to Co-dittmarite. When Co-pyrophosphates begin to crystallise at 400 °C (Fig. 2E and ESI: Fig. S3†), the crystal habit changes again to an elongated prism or a tabular habit. The single crystals form massive aggregates of tens of microns.

Tracking the removal of volatile components

As the phase composition and structure changed due to degassing (see eqn (1) and Fig. 1), we wanted to track the evaporation of the volatile components, mainly NH_3/H_2O, and the condensation of the phosphate environment, by performing

infrared (IR) and Raman spectroscopy (ESI: Supplementary Note 2 and Fig. S5†).

The IR and Raman bands correlate well with the phase compositions and the degrees of crystallinity of the Ni and Co samples [42,43]. The degree of crystallinity decreases in the *T*-series up to 300–400 °C due to the decomposition of the highly crystalline precursor M-struvite. It increases up to 800 °C during the crystallisation of Ni- and Co-pyrophosphates (Fig. 1). This trend is reflected in the progressive broadening and later narrowing/crystal field splitting of the phosphate stretching bands. Surprisingly, ammonium and water bands are still present at elevated temperatures of T = 400 °C, implying that these two species remain incorporated in the compounds.

The thermal effect on the coordination environment in the amorphous and crystalline Ni- and Co-phases

We further investigated the structures of amorphous and crystalline phases by following the changes/distortion in the metal coordination environment using X-ray absorption spectroscopy (XAS). Since XAS probes local coordination, it is particularly well-suited for establishing any potential differences among the structures of amorphous phases. Especially, the signal in the pre-peak region (X-ray absorption near-edge structure, XANES) contains information about the 1s-3d orbital transitions and expresses the degree of centrosymmetry of the first metal coordination sphere. Near-ideal centrosymmetric coordination shows very low pre-peak intensities, while more distorted geometries exhibit higher intensities. As only 3d-4p hybridisation enables parity-allowed transitions, the extent of those is strongly correlated with the coordination geometry. Due to an inversion centre, ideal octahedral coordination sites show lower pre-peak intensities than tetrahedral symmetries (A_{pp} = area of the pre-peak, $A_{pp}^{tetrahedral} > A_{pp}^{octahedral}$) (Fig. 3).

The signal beyond the absorption edge in the EXAFS region (extended X-ray absorption fine structure) depicts the excited photoelectron's interactions with the compound's next neighbour atoms. Here, the degree of crystallinity directly influences the signal's intensity and width. Since amorphous phases do not have an established long-range order, they show broader, and less intense peaks in the R-space mainly in the low

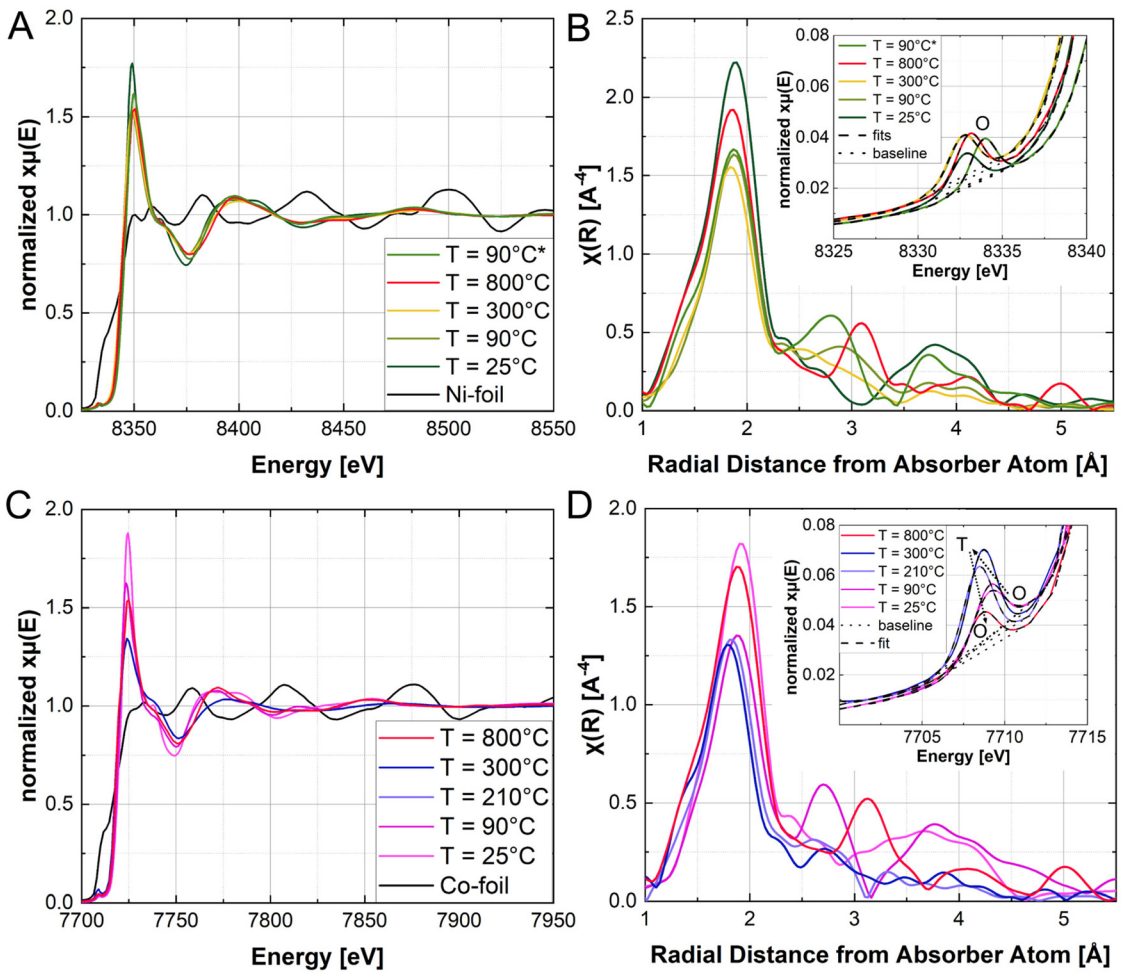

Fig. 3 XAS spectra of the thermally processed TMPs plotted in the real space and the R-space of (A and B) Ni-phosphates and (C and D) Co-phosphates; 90 °C* = hydrothermal synthesis at RH ≈ 100% at 90 °C. Inset in (B and D): pre-peak region and integration from Gaussian fits, O = octahedron, T = tetrahedron.

R-region due to an irregular arrangement of the lattice ions. The XAS spectra (Fig. 4) prove that Co and Ni are present exclusively as divalent M^{2+} species in all the samples (due to absorption edge at around 7730 and 8350 eV), as it is evidenced by comparing them with several M^{2+} standards (only metal foils are shown for the sake of clarity). Quantitative pre-peak integration results were calculated to compare the distortion in the first coordination sphere (ESI: Table S3†). The thermally induced change in the pre-peak area, indicative of a higher degree of distortion, differs significantly between the Ni- and Co-phosphate systems (Fig. 1). Up to 600 °C, crystalline Ni-struvite decomposes to an amorphous phase with a higher degree of distortion in remanent octahedral coordination [Ni: $A_{pp}^{25°C}$ = 0.028(2) (precursor), $A_{pp}^{300°C}$ = 0.034(2) and $A_{pp}^{600°C}$ = 0.041(2)]. In contrast, at low T < 200 °C the Co-system comprises crystalline octahedrally coordinated Co-phases, exhibiting a higher degree of distortion than the precursor Co-struvite [Co: $A_{pp}^{25°C}$ = 0.026(1), $A_{pp}^{90°C}$ = 0.032(1) and $A_{pp}^{150°C}$ = 0.041(2)]. In the further heating process due to the occurrence of a tetrahedrally coordinated Co-phase (NH_4CoPO_4) at T > 180 °C, the pre-peak intensity rises significantly [$A_{pp}^{210°C}$ = 0.071(1) and $A_{pp}^{300°C}$ = 0.075(3)]. When the crystallisation to $M_2P_2O_7$ (M = Ni, Co) occurs at T > 400 °C (for Ni at T = 600 °C, for Co at 400 °C), the pre-peak intensities in both systems decrease again. Here, the metal octahedra are still more distorted than those in the near-ideal octahedrally coordinated precursor M-struvites, which we associate with the presence of twisted and linked pyrophosphate chains ($A_{pp}^{800°C}$ (Ni and Co) = 0.033(1)).

Based on the fitting of the spectra in the R-space, radial distances from the absorber metal atom and average coordination numbers of the first coordination sphere could be calculated (ESI: Fig. S6–S8 and Tables S4–S20†). In the Ni-system, the calculated average coordination number, CN (*i.e.* degeneracy of oxygen), changes slightly from CN = 6.7(7) in the crystalline precursor Ni-struvite (T = 25 °C) to CN = 6.3(5) − 5.3(2) in the amorphous phase(s) (T = 90 °C–500 °C). Finally, Ni exhibits average coordination numbers of CN = 5.6(3) in the crystallised pyrophosphates, proving a remanent octahedral coordination with a slight degree of distortion in all occurring phases. The occurrence of several amorphous phases (polyamorphism) cannot be entirely ruled out. If this were the case, they all would have to exhibit similar local structures, as we do not observe any peak splitting in the Fourier-transformed spectra in R-space. In the Co-system the calculated average coordination number varies strongly from 6.4(5) in the precursor Co-struvite, to CN = 6.0(4) in Co-dittmarite heated at T = 90 °C to CN = 5.1(3) in the phase mixture of NH_4CoPO_4, $HCoPO_4{\cdot}H_2O$, an amorphous phase and residues of Co-dittmarite heated at 210 °C. Finally, at 300 °C, the average coordination number of Co decreases to a value of CN = 3.6(2), indicative for a tetrahedral coordination. When the crystallisation of $Co_2P_2O_7$ begins at ≥400 °C, the coordination number increases again to a value near 6 (CN = 5.3(4) at 400 °C and CN = 5.6(6) at 800 °C), which suggests octahedral coordination. In this way, the anticipated phase-dependent coordination transitions from octahedral ($NH_4CoPO_4{\cdot}6H_2O$, $NH_4CoPO_4{\cdot}H_2O$,

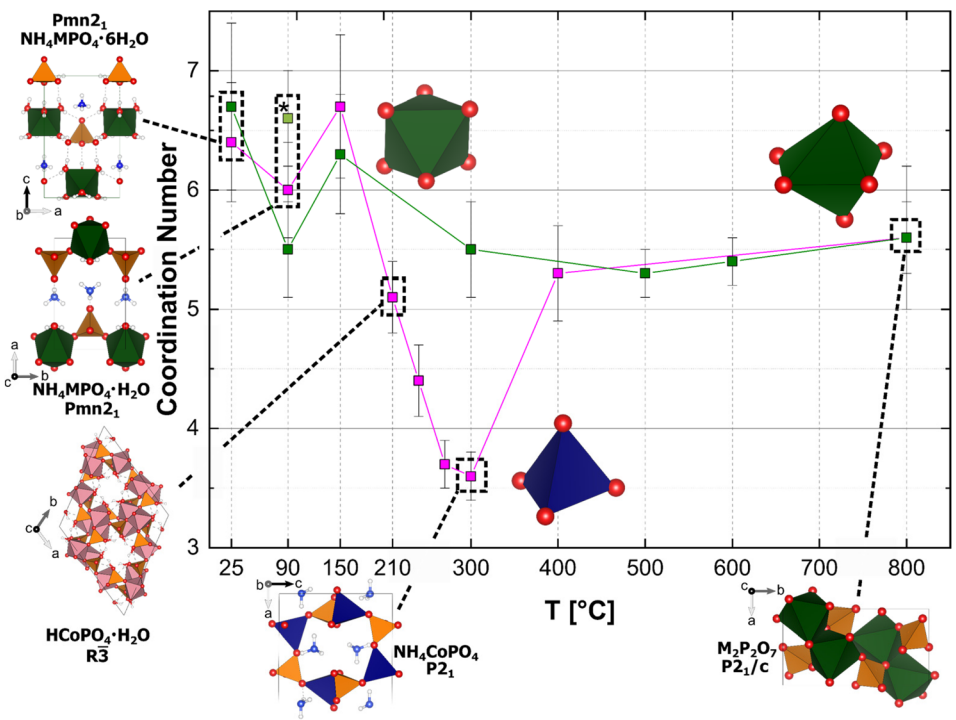

Fig. 4 Calculated coordination numbers through the thermal history of Ni (green squares)- and Co (pink squares)-phosphate compounds; Occurring phases with their crystal structure in tetrahedral and octahedral coordination are depicted. The asterisk marks the hydrothermal synthesised Ni-dittmarite compound.

HCoPO4·H_2O) to tetrahedral (NH_4CoPO_4), and back to octahedral ($Co_2P_2O_7$) could be successfully derived by fitting EXAFS spectra in the R-space.

Our EXAFS characterisation and observations from other methods paint a coherent image of changes in metal coordination, correlating with the phase compositions. These results are summarised in Fig. 4. Here the degeneracy of oxygen, *i.e.* the distinct metal's calculated coordination number (CN), is plotted against the processed temperature. A change in the coordination geometry causes the intense colour change of Co in the heated samples from an octahedral one in [CoO_6] (NH_4CoPO_4·$6H_2O$, NH_4CoPO_4·H_2O, HCoPO4·H_2O, amorphous phase, see also Fig. 1) to a tetrahedral one in [CoO_4] (NH_4CoPO_4) and again to an octahedral coordination environment ($Co_2P_2O_7$). Due to an increasing Jahn–Teller effect as Co^{2+} is no longer coordinated by six O^{2-} of H_2O molecules but by five O^{2-} of PO_4 and one remaining O^{2-} from H_2O, a color change can be observed from pink (Co-struvite) to purple (Co-dittmarite). When heated at 210 °C, Co-dittmarite transforms into $HCoPO_4$·H_2O and secondly into NH_4CoPO_4 accompanied by an intense colour change from purple to "cobalt blue". The analogous colour change caused by an octahedral-tetrahedral coordination change was also observed in the related potassium compound of $KCoPO_4$·H_2O and $KCoPO_4$.[44] Here, the degree of distortion increases even more indicated by an increase in pre-peak area due to a Co^{2+} coordination change from an octahedron to a tetrahedron. The associated change in d-orbital splitting with a change in coordination significantly affects the colour of the Co-compounds. When the coordination switches again to an octahedral configuration accompanied by the phase transformation of NH_4CoPO_4 to $Co_2P_2O_7$, the CoO_6 octahedron in Co-pyrophosphate exhibits a lower degree of distortion than the CoO_4 tetrahedron in NH_4CoPO_4. Therefore, the pre-peak area decreases while the intensity of the white line increases again (Fig. 4). Based on the calculations on the degeneracy, Co^{2+} has a near octahedral coordination in the amorphous compound. Due to their presence in the *T*-range of 210–500 °C, a low amount of Co is always bound in octahedral coordination.

From the crystal field stabilisation energy (CFSE) perspective, Ni^{2+} as a d^8 ion strongly prefers octahedral coordination. The difference in CFSE between tetrahedral and octahedral geometries is significantly higher ($|\Delta CFSE_{O-T}|$ = 0.84 with $CFSE_O$ = −1.2 Δ_O, $CFSE_T \approx -0.36\ \Delta_O$ assuming $\Delta_T = 4/9\ \Delta_O$[45]) than the difference between both geometries in the Co-system. Co^{2+} as a d^7 ion exhibits only a slight difference between the $CFSE_O$ and $CFSE_T$ in high spin configurations ($|\Delta CFSE_{O-T}|$ = 0.27 with $CFSE_O$ = −0.8 Δ_O and $CFSE_T \approx -0.53\ \Delta_O$). This difference in energy/stability in comparison with Ni^{2+} promotes an additional occurrence of tetrahedral coordination in the Co-system.[46,47]

Summarised order of phase transitions with increasing temperature

Based on the combined multi-modal characterisation, we established the order of phase transitions in our M-struvite systems. At first, Ni-struvite decomposes to an amorphous phase while Co-struvite transforms through a crystalline-crystalline phase transition to Co-dittmarite at *T* = 90 °C (Fig. 1). The pseudomorphic phase transition of the amorphous Ni-PO_4 phase formed from Ni-struvite, leads to a relict "Ni-struvite crystal skeleton" visible in the SE images (ESI: Fig. S2†). Although pseudomorphism indicates a weak degree of densification and structural reconfiguration (otherwise precursor crystal framework would collapse), the relict crystal morphology is not in every case preserved as in the 500 °C sample (ESI: Fig. S2K†). Looking at the degassing events of heated Co-struvite based on XRD and DSC, an amorphous phase formed in a second and third thermal event at 140 °C and 250 °C, associated with the partial decomposition of Co-dittmarite and $HCoPO_4$·H_2O (Fig. 1). The amorphous phase is proposed to be akin to $HCoPO_4$ based on the TGA/DSC, as is also suggested by other studies in the literature[48,49] Surprisingly, ammonia is still present in the amorphous phases up to 400 °C in both metal systems, which is important for potential proton carrier molecules. Based on the EXAFS fits, the spectra of the amorphous phases *T* > 400 °C resemble mostly those of crystalline Ni-pyrophosphate with less pronounced long-range order above *R* distances > 4 Å. This fact indicates a beginning of pyrophosphatisation already at 400 °C in agreement with FT-IR and FT-RS. Further heating leads to the actual crystallisation of M-pyrophosphate. At 400 °C $Co_2P_2O_7$ forms, although a major proportion of amorphous phases is present. In contrast, the amorphous nickel phosphate phase remains stable up to 600 °C until it converts to $Ni_2P_2O_7$. The humidity and heating time/rate can significantly influence the phase stability and crystallinity, especially in the low *T*-region below 400 °C. This ability of M-struvite to sequentially convert into various amorphous and crystalline transition metal phosphate phases opens the space for possible crystal and phase engineering and upcycling of the waste-derived struvite[29,40,50,51] into tailored TMPs, as we indeed explore below.

Proton conducting properties of selected Ni- and Co-phosphates

The structural results presented above point to the potential presence of extensive hydrogen-bonded frameworks involving the coordination of water H_2O and ammonia NH_3 molecules in some of the amorphous or crystalline TMP phases of Ni and Co. Such frameworks indicate a potential for good proton conductive properties of these compounds. To characterise our processed TMP phases as functional proton conductive materials, proton conductivity (PC) measurements were performed on the pressed powder pellets at different relative humidity values and temperatures (Fig. 5, see Methods Proton conductivity measurements for more details, Fig. S9–S11†). Before and after each PC measurement, a diffraction pattern was recorded to demonstrate the phase stability (Fig. S12†). The impedance spectra were fitted with a minimal circuit model consisting of a parallel constant phase element (CPE) and resistor (R) in series with two parallel Warburg elements (W_S and W_O, inset: Fig. 5B).

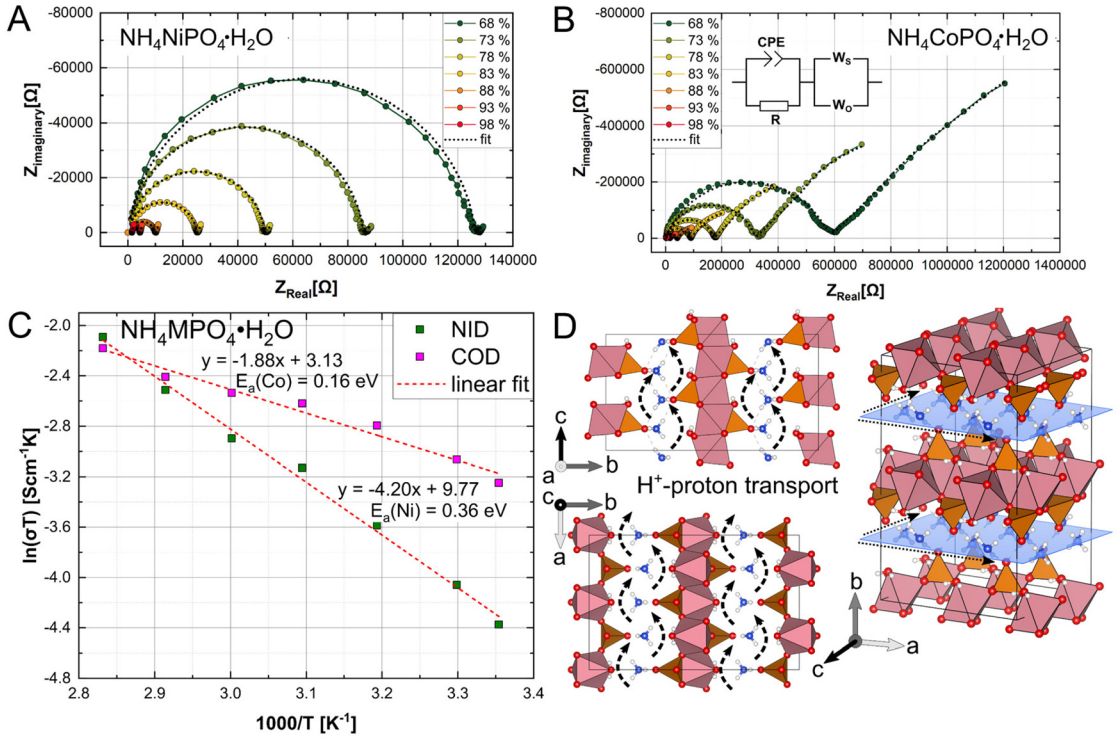

Fig. 5 Nyquist plots with real and imaginary impedance of (A) Ni- and (B) Co-dittmarite, $NH_4MPO_4{\cdot}H_2O$ with M = Ni, Co at RH = 68%–98% at T = 25 °C; inset in B: equivalent circuit of the fitting model; (C) Arrhenius plots of Ni- and Co-dittmarite with ln (σT) *vs.* 1000/T [K^{-1}] (T = 25 °C–80 °C), red dashed line = fit of the data; inset: DVS isotherms of Ni- and Co-dittmarite; (D) view on the (0k0) plane of the crystal structure of M-dittmarite *Pmn*2$_1$ from different perspectives; dashed black arrows and blue marked (0k0) planes indicate enhanced proton migration pathways.

The high-frequency R-CPE circuit represents the electronic resistivity of the metal phosphate phase. In our model, the low-frequency W_S–W_O circuit models the effects of the proton transport through grain boundaries. The Warburg short element expresses the transmissive, while the Warburg open element points to the reflective character of the grain boundary. No singular Warburg element (either a general, short or open W), fitted the impedance spectra sufficiently well. Including two Warburg elements resulted in much more accurate fitting results. From the intersection of the fits and the abscissa axis (real part of impedance Z'), the proton conductivity was calculated (more details in ESI: Methods proton conductivity measurements†). As the current is measured perpendicularly to the pellet base, the proton conductivity is interpreted as bulk proton conductivity under the assumption of randomly orientated grain boundaries.[52] The activation energy (E_A) of proton migration is the amount of energy required for a proton to jump from one ionic domain to another, an important value to distinguish between Grotthuss and vehicle mechanism.

Selected samples of the Ni- and Co T-series (Fig. 1) were analysed. For Co: Co-dittmarite processed at T = 90 °C, NH_4CoPO_4 at T = 300 °C and Co-pyrophosphate at T = 800 °C. For Ni: Ni-dittmarite at T = 90 °C in 100% H_2O, amorphous Ni-PO_4 at T = 500 °C and Ni-pyrophosphate at T = 800 °C. All data and fits associated with the proton conductivity are summarised in the ESI (Fig. S9–S11 and Tables S22, S23†). The electrochemical impedance data were plotted in Nyquist diagrams with the imaginary part of the impedance on the y-axis $Z_{imaginary}$ and the real part of the impedance on the x-axis Z_{real}. All Nyquist plots demonstrate semicircles in the high-frequency region and an elongated tail in the low-frequency region. The M-dittmarite compounds of Ni and Co, heated at T = 90 °C and stable up to 200 °C, exhibit the highest proton conductivities of all analysed phases at 1.4×10^{-4} S cm^{-1} and 4.2×10^{-5} S cm^{-1} for Co- and Ni-dittmarite, respectively, at RH = 98% and T = 25 °C. Considering the low-frequency region, the Warburg coefficients from the fits show a slight increase of the W_S/W_O ratio with higher RH, visible in both M-dittmarite components from nearly near zero to 2.5(1) for Ni and 6.5(9) for Co (ESI: Table S23†). This could indicate a more transmissive nature of the grain boundaries at high RH. From a crystallographic point of view, protons can "jump" in the hydrogen-bond network mainly in the (0k0) plane in two directions, where ammonium NH_4 and the coordinating water of the metal octahedron are located.

Since protons are most likely transported through 2D layers, build up by the ammonium sites (Fig. 5) in the M-dittmarite structure *Pmn*2$_1$, the compound probably demonstrates a significant anisotropic proton conductivity in directions in the (010) plane. Perpendicularly to this direction, the proton conductivity is most likely decreasing. As we measured the bulk proton conductivity of a pressed pellet of the material, grain boundaries, microstructure and the orientation of the different grains effect the overall bulk properties. Due to these

anisotropic features, the overall bulk proton conductivity could be influenced. Furthermore, to evaluate the water affinity and adsorption, a major factor influencing the proton conductivity, dynamic vapour sorption (DVS) measurements were carried out (inset in Fig. 6C and ESI: Fig. S11†). Co-dittmarite displays a final water uptake of 0.0263 $cm^3\ g^{-1}$ at RH = 98%, corresponding to the sorption of 0.27 H_2O molecules per formula unit. Ni-dittmarite exhibits lower values of 0.0164 cm^3 H_2O/g at 98% RH equating to 0.17 molecules of H_2O per formula unit. However, for all the RH values and T = 25 °C, the Co compound exhibits proton conductivities around one order of magnitude higher than those found for the Ni analogue. This discrepancy disappears with higher temperatures up to 80 °C (Fig. 6C). Although both compounds share the same structure, Co^{2+} exhibits higher proton conductivity at T = 25 °C in Co-dittmarite, which can be correlated with slight structural differences compared to Ni-dittmarite, as indicated by our XAS measurements. The differences in bond lengths, especially of the first coordination sphere Co–O and Ni–O could cause different local polarities resulting in a changed proton mobility (ESI: Tables S11 and S13†). The adsorbed amount of water could only promote an increase of proton conductivity at high RH > 80%, but not at lower RH ≤ 80%. The dependency of the proton conductivity on the water partial pressure (associated with the RH) is similar for both dittmarite phases, because their $\log(\sigma)$ *vs.* $\log(pH_2O)$ slope values are relatively close to each other (16 ± 2 (Ni) *vs.* 13 ± 1 (Co), Table S22†). When examining other processed phosphate phases, NH_4CoPO_4 shows a significant proton conductivity of 6.42×10^{-5} S cm^{-1} at RH = 98% and T = 80 °C. The other phases, $Ni_2P_2O_7$, $Co_2P_2O_7$ and the amorphous Ni-PO_4 phase of heated at 500 °C, demonstrate low to medium proton conductivities in the range of 10^{-6}–10^{-7} S cm^{-1} (ESI: Fig. S8 and S9†). The M-dittmarite and $M_2P_2O_7$ phases did not change its phase composition after the PC measurement, while the amorphous Ni-phase and NH_4CoPO_4 crystallised. In addition, the water partial pressure-dependent proton conductivity behaviour of the $M_2P_2O_7$ compounds is significantly different from that of Ni-, Co-dittmarite, and NH_4CoPO_4. Due to a highly condensed structure, the adsorbed water in the pyrophosphates, even at high RH (>85%), does not provide a significant jump in proton conductivity (ESI: Fig. S10 and Table S22†).

This work's goal was to obtain a TMP material with high thermal stability and significant proton conductivity optimal for their potential applicational use, *e.g.*, proton exchange membranes in fuel cells (Fig. 1). For this purpose, the mechanism of ionic conductivity/proton migration in the material had to be investigated by determining its activation energy. In general, proton conductivity is assumed to rely on two major transport mechanisms, the Grotthuss mechanism and the vehicle mechanism.[53] The Grotthuss mechanism *i.e.* proton jumping, points to the migration processes of protons through translation from an $H_{2n+1}O_n^+$ ion to a water molecule by tunnelling in a hydrogen bond with subsequent molecule rotation. This diffusing proton in the newly formed $H_{2n+1}O_n^+$ ion can attach to the next neighbour water molecules resulting in a successive motion of H^+ over small molecular distances through the compound.[53,54] Recent O–K-edge XAS results could prove the dominant occurrence of an $H_7O_3^+$ proton complex in contrast to the conventional explanation of Zundel or Eigen ions, $H_5O_2^+$ and $H_9O_4^+$.[55] In the vehicle mechanism, molecules such as water H_2O, ammonia NH_3, or alkali metals Na, K, *etc*. act as proton acceptors/Brønsted bases and transport the protons as carriers through the compound over large molecular distances.[53] The activation energy of proton migration E_A, calculated from the Arrhenius plots, is a key parameter to distinguish between those mechanisms.[53,56] A value between 0.1–0.4 eV per proton indicates proton jumping, meaning the transfer of protons is accomplished between the proton donor and acceptor. A value greater than 0.4 eV per particle implies a vehicle mechanism where a proton transport proceeds *via* the diffusion of protonated carriers.[52,53] A low content of ammonia and water in the compound resulting from heating at elevated temperatures would decrease the proton conductivity performance as a weaker hydrogen-bond network and a lower number of potential carriers of protons are available. The crystal structure determines the possibilities and pathways for preferential proton transport *e.g.* through 1D channels, 2D layers, or 3D frameworks, and the binding strength of the hydrogen network (*e.g.* "free" crystal water *vs.* bound hydroxyl groups). Therefore, the absolute number of protons and carrier molecules in the structure and the internal structure significantly influence the overall PC performance. The dittmarite structure $Pmn2_1$ seems to provide a beneficial structure for enhanced proton conduction as protons can migrate through the weakly bound ammonium layers in two dimensions. The increase of the Warburg ratio W_S (transmissive boundary)/W_O (reflective boundary) with increasing RH could represent a more transmissive behaviour of the grain boundaries as interpreted by other studies.[57–59] More water units are adsorbed at the interfaces providing an enhanced proton transfer due to a higher density of potential transporting molecules. The calculated values for the activation energy E_A infer a Grotthuss mechanism (<0.4 eV) in most compounds except for the Ni- and Co-pyrophosphates. In these compounds, no structural water or ammonia are present, and carrier molecules only accomplish proton conduction, indicated by the high activation energy E_A and the slopes of $\log(\sigma)$ *vs.* $\log(pH_2O)$ (ESI: Table S22†). The similar increase of proton conductivity of Ni- and Co-dittmarite at higher RH/partial pressures of water majorly agrees with the uptake of water visible in the DVS isotherms and the slopes of $\log(\sigma)$ *vs.* $\log(pH_2O)$ (Fig. 6 and ESI: Fig. S9–S11, Table S22†). The activation energies for proton migration of 0.16 eV for Co-dittmarite and 0.36 eV for Ni-dittmarite are relatively low compared to other oxides and phosphate compounds (Table 1 and ESI: Table S23†).

In addition, based on recent research,[60] the dittmarite structure shows high suitability as a framework crystal for high-entropy phosphate materials (HEMPs). HEMPs are known to be electrochemically more active than their pure endmembers as the high configurational entropy of mixing

Table 1 Summarized proton conductivity data of most promising metal phosphate compounds. o.w. = our work

Material	Chemical composition	T [°C]/RH [%]	σ [S cm^{-1}]	E_a (eV)	Ref.
Ionomer	NAFION®	25/98	7.80×10^{-2}	—	63
Na-Al-PO_4	$Na_6[(AlPO_4)_8(OH)_6]\cdot 9H_2O$	20/98	3.60×10^{-3}	0.21	64
Doped $Sn_2P_2O_7$	$In_{0.1}Sn_{0.9}P_2O_7$	300/—	0.195	—	65
Sn-PO_4	$Sn(HPO_4)_2\ 3H_2O$	100/—	1.00×10^{-2}	—	27
ZrP_2O_7	$Zr(P_2O_7)_{0.81}(O_3POH)_{0.38}$	20/98	1.30×10^{-3}	—	25
TiP_2O_7	TiP_2O_7	100/—	4.40×10^{-3}	0.14	66
Ti-PO_4	$Ti_2(HPO_4)_4$	20/95	1.20×10^{-3}	0.13	67
org./inorg. Mn-PO_4-comp.	$(C_2H_{10}N_2)$ $[Mn_2(HPO_4)_3](H_2O)$	20/99	1.60×10^{-3}	0.22	68
org./inorg. Fe-PO_4-comp.	$(C_4H_{12}N_2)_{1.5}[Fe_2(OH)(H_2PO_4)(HPO_4)_2(PO_4)]$ $0.5(H_2O)$	40/98	5.10×10^{-4}	—	69
org./inorg. Co-PO_4-comp.	$(C_2N_2H_{10})_{0.5}CoPO_4$	56/98	2.00×10^{-3}	1.01	70
org./inorg. Zn-PO_4-comp.	$NMe_4Zn[HPO_4][H_2PO_4]$	30/98	1.30×10^{-2}	0.92	71
K-V-PO_4	$K_2[(VO)_2(HPO_4)_2(C_2O_4)]$	40/95	1.15×10^{-2}	—	72
NH_4-Ni-PO_4	$NH_4NiPO_4\ H_2O$	25/98	4.20×10^{-5}	0.36	o.w.
NH_4-Co-PO_4	$NH_4NiPO_4\ H_2O$	25/98	1.40×10^{-4}	0.16	o.w.

promotes their reactivity.[61,62] In such a way, a high-entropy transition metal dittmarite compound derived from a high-entropy struvite could show even better performance than Ni- or Co in proton conductivity, but this aspect has to be further evaluated.

Finally, we showed in our previous study,[40] that M-struvite could be precipitated from industrial wastewater. Here we demonstrate that through a simple thermal treatment, these reclaimed TMP materials could be upcycled for applicational purposes (Fig. 1). The processed M-dittmarite compounds of Ni- and Co demonstrate high to superprotonic conductive behaviour comparable to ionomers, *i.e.* Nafion 117,[63,73,76] MOFs,[74] perovskites,[75]or other oxide/phosphate compounds.

A summary of selected high-performing proton conductive transition metal phosphate compounds can be found in Table 1 in further detail in the ESI (Table S23†).While most of the reported compounds require a complex multistep synthesis, our as-obtained materials could be precipitated in a facile one pot way directly out of wastewater. For example, ceramic oxide proton conductors, often perovskite-type, require in most cases an energy intensive, and complex solid state or solvothermal syntheses. Even if the absolute bulk proton conductivity values of the as-obtained Ni-and Co-dittmarites are not among the highest measured, they are still sufficiently conductive considering that we are discussing recycled waste materials. Due to their high thermal and chemical stability up to 210 °C, the M-dittmarite compounds could endure the optimal operating temperatures in conventional fuel cells. These compounds may be upcycled directly or could be reused indirectly by processing them even further to an advanced proton conductive material. In combination with their high compatibility with other cell components (electrodes, electrolytes, seals) and low cost, M-dittmarites are promising proton-conducting materials.[77,78]

Conclusions

In this study, we followed the thermal history of Ni- and Co-struvite decomposition all the way to their crystallisation into M-pyrophosphates. Ni-struvite forms an amorphous phase during the thermal treatment, which preserves octahedral metal coordination with slight distortion at all temperatures. The complex amorphous structure increasingly resembles a local structure of a Ni-pyrophosphate with progressive temperatures. In contrast, heated Co-struvite exhibits several crystalline-crystalline phase transitions with an associated change of metal coordination from octahedral to tetrahedral, and back to octahedral. In both systems, volatile compounds such as H_2O or NH_3 are still present in the solids up to 400 °C, potentially making transition metal phosphates promising high-temperature water-retaining materials. The metal and phosphate coordination environment associated with the amount of bound water and ammonia in the thermally treated TMPs could be directly linked to their proton conductivity performance. Indeed, with values of $>10^{-4}$ S cm^{-1} at room temperature, a low activation energy of 0.16 eV, and high thermal stability above 200 °C, the layered Ni- and Co-dittmarites are the most promising candidates as proton exchange material, among all the obtained phases. Importantly, we showed that such functional materials could be directly made by thermally processing M-struvites, which might be precipitated from various wastewater streams.

Conflicts of interest

There are bo conflicts do declare.

Acknowledgements

We acknowledge Dr Martin Radtke (BAM) for his help at the BAMline beamline of BESSY II. We thank BAM and Helmholtz-Zentrum Berlin (HZB) for providing us with the beamtime at BESSY II. We thank Dr Thomas Schmidt for providing us access to the Raman microscope.

References

1 Y. Zhao, Z. Chen, D. B. Xiong, Y. Qiao, Y. Tang and F. Gao, Hybridized Phosphate with Ultrathin Nanoslices and Single Crystal Microplatelets for High Performance Supercapacitors, *Sci. Rep.*, 2016, **6**, 17613.

2 W.-X. Lu, B. Wang, W.-J. Chen, J.-L. Xie, Z.-Q. Huang, W. Jin and J.-L. Song, Nanosheet-like Co3(OH)2(HPO4)2 as a Highly Efficient and Stable Electrocatalyst for Oxygen Evolution Reaction, *ACS Sustainable Chem. Eng.*, 2019, **7**, 3083–3091.

3 J. Zhang, Y. Yang, Z. Zhang, X. Xu and X. Wang, Rapid synthesis of mesoporous NixCo3−x(PO4)2hollow shells showing enhanced electrocatalytic and supercapacitor performance, *J. Mater. Chem. A*, 2014, **2**, 20182–20188.

4 X. Li, P. Xu, M. Chen, G. Zeng, D. Wang, F. Chen, W. Tang, C. Chen, C. Zhang and X. Tan, Application of silver phosphate-based photocatalysts: Barriers and solutions, *Chem. Eng. J.*, 2019, **366**, 339–357.

5 W. Zhang, P. Oulego, S. K. Sharma, X. L. Yang, L. J. Li, G. Rothenberg and N. R. Shiju, Self-Exfoliated Synthesis of Transition Metal Phosphate Nanolayers for Selective Aerobic Oxidation of Ethyl Lactate to Ethyl Pyruvate, *ACS Catal.*, 2020, **10**, 3958–3967.

6 D. Zhang, H. Qiu, L. Jiang, F. Lv, C. Ma and W. Hu, Enantioselective palladium(II) phosphate catalyzed three-component reactions of pyrrole, diazoesters, and imines, *Angew. Chem., Int. Ed. Engl.*, 2013, **52**, 13356–13360.

7 M. Chen, X. Fu, Z. Chen, J. Liu and W. H. Zhong, Protein–Engineered Functional Materials for Bioelectronics, *Adv. Funct. Mater.*, 2021, **31**, 2006744.

8 N. Omar, M. A. Monem, Y. Firouz, J. Salminen, J. Smekens, O. Hegazy, H. Gaulous, G. Mulder, P. Van den Bossche, T. Coosemans and J. Van Mierlo, Lithium iron phosphate based battery – Assessment of the aging parameters and development of cycle life model, *Appl. Energy*, 2014, **113**, 1575–1585.

9 B. Senthilkumar, Z. Khan, S. Park, I. Seo, H. Ko and Y. Kim, Exploration of cobalt phosphate as a potential catalyst for rechargeable aqueous sodium-air battery, *J. Power Sources*, 2016, **311**, 29–34.

10 Q. Liu, L. Zhou, D. Zhao, C. Wan, P. Sun, X. Lv, X. Sun and L. Fang, Constructing aqueous rechargeable Zn//Co battery with hierarchical structural cobalt phosphate octahydrate for high-performance energy storage, *J. Power Sources*, 2022, **533**, 231344.

11 J. Hassoun, F. Bonaccorso, M. Agostini, M. Angelucci, M. G. Betti, R. Cingolani, M. Gemmi, C. Mariani, S. Panero, V. Pellegrini and B. Scrosati, An Advanced Lithium-Ion Battery Based on a Graphene Anode and a Lithium Iron Phosphate Cathode, *Nano Lett.*, 2014, **14**, 4901–4906.

12 N. L. W. Septiani, Y. V. Kaneti, K. B. Fathoni, K. Kani, A. E. Allah, B. Yuliarto, Nugraha, H. K. Dipojono, Z. A. Alothman, D. Golberg and Y. Yamauchi, Self-Assembly of Two-Dimensional Bimetallic Nickel–Cobalt Phosphate Nanoplates into One-Dimensional Porous Chainlike Architecture for Efficient Oxygen Evolution Reaction, *Chem. Mater.*, 2020, **32**, 7005–7018.

13 L. Xie, R. Zhang, L. Cui, D. Liu, S. Hao, Y. Ma, G. Du, A. M. Asiri and X. Sun, High-Performance Electrolytic Oxygen Evolution in Neutral Media Catalyzed by a Cobalt Phosphate Nanoarray, *Angew. Chem., Int. Ed.*, 2017, **56**, 1064–1068.

14 M. Pramanik, C. Li, M. Imura, V. Malgras, Y. M. Kang and Y. Yamauchi, Ordered Mesoporous Cobalt Phosphate with Crystallized Walls toward Highly Active Water Oxidation Electrocatalysts, *Small*, 2016, **12**, 1709–1715.

15 K. Otsuka and Y. Wang, Direct conversion of methane into oxygenates, *Appl. Catal., A*, 2001, **222**, 145–161.

16 N. Brodt and J. Niemeyer, Chiral organophosphates as ligands in asymmetric metal catalysis, *Org. Chem. Front.*, 2023, DOI: 10.1039/D3QO00206C.

17 J. De Maron, L. Bellotti, A. Baldelli, A. Fasolini, N. Schiaroli, C. Lucarelli, F. Cavani and T. Tabanelli, Evaluation of the Catalytic Activity of Metal Phosphates and Related Oxides in the Ketonization of Propionic Acid, *Sustain. Chem.*, 2022, **3**, 58–75.

18 A. Matsuda, H. Tateno, K. Kamata and M. Hara, Iron phosphate nanoparticle catalyst for direct oxidation of methane into formaldehyde: effect of surface redox and acid–base properties, *Catal. Sci. Technol.*, 2021, **11**, 6987–6998.

19 R. Lin and Y. Ding, A Review on the Synthesis and Applications of Mesostructured Transition Metal Phosphates, *Materials*, 2013, **6**, 217–243.

20 H. Zhao and Z. Yuan, Insights into Transition Metal Phosphate Materials for Efficient Electrocatalysis, *ChemCatChem*, 2020, **12**, 3797–3810.

21 H. Mohammed, A. Al-Othman, P. Nancarrow, Y. Elsayed and M. Tawalbeh, Enhanced proton conduction in zirconium phosphate/ionic liquids materials for high-temperature fuel cells, *Int. J. Hydrogen Energy*, 2021, **46**, 4857–4869.

22 J. Pandey, M. M. Seepana and A. Shukla, Zirconium phosphate based proton conducting membrane for DMFC application, *Int. J. Hydrogen Energy*, 2015, **40**, 9410–9421.

23 Y. Kawakami and M. Miyayama, Proton Conducting Properties of Layered Metal Phosphate Hydrates, *Key Eng. Mater.*, 2006, **320**, 267–270.

24 K. P. Ramaiyan, S. Herrera, M. J. Workman, T. A. Semelsberger, V. Atanasov, J. Kerres, S. Maurya, Y. S. Kim, C. R. Kreller and R. Mukundan, Role of phosphate source in improving the proton conductivity of tin pyrophosphate and its composite electrolytes, *J. Mater. Chem. A*, 2020, **8**, 16345–16354.

25 G. Alberti, M. Casciola, S. Cavalaglio and R. Vivani, Proton conductivity of mesoporous zirconium phosphate pyrophosphate, *Solid State Ionics*, 1999, **125**, 91–97.

26 P. V. Valsaraj and C. Janardanan, Comparative studies on Proton conducting nature of Copper selective tin Zirconium phosphate Cation exchanger with its single Salts counter parts, *Res. J. Chem. Sci.*, 2014, **4**, 84–90.

27 W. Huang, S. Komarneni, Y. D. Noh, J. Ma, K. Chen, D. Xue, X. Xue and B. Jiang, Novel inorganic tin phosphate

gel: multifunctional material, *Chem. Commun.*, 2018, **54**, 2682–2685.
28 D. Shakhvorostov, M. A. Nicholls, P. R. Norton and M. H. Müser, Mechanical properties of zinc and calcium phosphates, *Eur. Phys. J. B*, 2010, **76**, 347–352.
29 S. Karafiludis, A. G. Buzanich, C. Heinekamp, A. Zimathies, G. J. Smales, V.-D. Hodoroaba, J. E. ten Elshof, F. Emmerling and T. M. Stawski, Template-free synthesis of mesoporous, amorphous transition metal phosphate materials, *Nanoscale*, 2023, **15**, 3952–3966.
30 G. Renaudin, S. Gomes and J. M. Nedelec, First-Row Transition Metal Doping in Calcium Phosphate Bioceramics: A Detailed Crystallographic Study, *Materials*, 2017, **10**, 92.
31 E. Mahboubi, A. Yourdkhani and R. Poursalehi, Liquid phase deposition of iron phosphate thin films, *CrystEngComm*, 2018, **20**, 5256–5268.
32 R. M. P. Colodrero, P. Olivera-Pastor, A. Cabeza and M. Bazaga-Garcia, Properties and Applications of Metal Phosphates and Pyrophosphates as Proton Conductors, *Materials*, 2022, **15**, 1292.
33 P. P. Prosini, L. Cianchi, G. Spina, M. Lisi, S. Scaccia, M. Carewska, C. Minarini and M. Pasquali, Synthesis and Characterization of Amorphous 3Fe2O3·2P2O5·10H2O and Its Electrode Performance in Lithium Batteries, *J. Electrochem. Soc.*, 2001, **148**, A1125.
34 O. Delmer, P. Balaya, L. Kienle and J. Maier, Enhanced Potential of Amorphous Electrode Materials: Case Study of RuO2, *Adv. Mater.*, 2008, **20**, 501–505.
35 K. S. Le Corre, E. Valsami-Jones, P. Hobbs and S. A. Parsons, Phosphorus Recovery from Wastewater by Struvite Crystallization: A Review, *Crit. Rev. Environ. Sci. Technol.*, 2009, **39**, 433–477.
36 A. Uysal, Y. D. Yilmazel and G. N. Demirer, The determination of fertilizer quality of the formed struvite from effluent of a sewage sludge anaerobic digester, *J. Hazard. Mater.*, 2010, **181**, 248–254.
37 X. Hao, C. Wang, M. C. van Loosdrecht and Y. Hu, Looking beyond struvite for P-recovery, *Environ. Sci. Technol.*, 2013, **47**, 6–4965.
38 M. Sena, M. Seib, D. R. Noguera and A. Hicks, Environmental impacts of phosphorus recovery through struvite precipitation in wastewater treatment, *J. Cleaner Prod.*, 2021, **280**, 124222.
39 Z. Song, K. C. Wang, Q. Sun, L. Zhang, J. Li, D. Li, P. W. Sze, Y. Liang, X. Sun, X. Z. Fu and J. L. Luo, High-Performance Ammonium Cobalt Phosphate Nanosheet Electrocatalyst for Alkaline Saline Water Oxidation, *Adv. Sci.*, 2021, **8**, 2100498.
40 S. Karafiludis, A. G. Buzanich, Z. Kochovski, I. Feldmann, F. Emmerling and T. M. Stawski, Ni- and Co-Struvites: Revealing Crystallization Mechanisms and Crystal Engineering toward Applicational Use of Transition Metal Phosphates, *Cryst. Growth Des.*, 2022, **22**, 4305–4315.
41 E. T. Pedrosa, C. V. Putnis and A. Putnis, The pseudomorphic replacement of marble by apatite: The role of fluid composition, *Chem. Geol.*, 2016, **425**, 1–11.
42 L. Popovi, D. de Waal and J. C. A. Boeyens, Correlation between Raman wavenumbers and P-O bond lengths in crystalline inorganic phosphates, *J. Raman Spectrosc.*, 2005, **36**, 2–11.
43 K. D. Litasov and N. M. Podgornykh, Raman spectroscopy of various phosphate minerals and occurrence of tuite in the Elga IIE iron meteorite, *J. Raman Spectrosc.*, 2017, **48**, 1518–1527.
44 Q. Che, X. Xie, Q. Ma, J. Wang, Y. Zhu, R. Shi and P. Yang, Coordination environment evolution of Co(ii) during dehydration and re-crystallization processes of $KCoPO4{\cdot}H_2O$ towards enhanced electrocatalytic oxygen evolution reaction, *RSC Adv.*, 2020, **10**, 14972–14978.
45 E. Larsen and G. N. L. Mar, The angular overlap model. How to use it and why, *J. Chem. Educ.*, 1974, **51**, 8.
46 H. Irving and R. Williams, Order of stability of metal complexes, *Nature*, 1948, **162**, 746–747.
47 H. Irving and R. Williams, The stability of transition-metal complexes, *J. Chem. Soc.*, 1953, 3192–3210, DOI: **10.1039/JR9530003192**.
48 D. Choi, X. Li, W. A. Henderson, Q. Huang, S. K. Nune, J. P. Lemmon and V. L. Sprenkle, LiCoPO4 cathode from a $CoHPO4.xH_2O$ nanoplate precursor for high voltage Li-ion batteries, *Heliyon*, 2016, **2**, e00081.
49 H. Zhang, Y. Lu, X. Jin, B. Wang, T. Yang, H. Xu, H. Liu and C. Chao, A facile and gentle method to fabricate NH4CoPO4 coating with superhydrophobic character study, *Mater. Res. Express*, 2019, **6**, 105044.
50 X. Lu, Z. Huang, Z. Liang, Z. Li, J. Yang, Y. Wang and F. Wang, Co-precipitation of Cu and Zn in precipitation of struvite, *Sci. Total Environ.*, 2021, **764**, 144269.
51 R. Zhangchen, W. G. Liu, Q. H. Ji, Y. Li, J. Zhang, J. Song, Y. Zhong and L. Zhou, Struvite as seed materials for treatment of heavy metals in wastewater, *IOP Conf. Ser.: Earth Environ. Sci.*, 2021, **770**, 1–5.
52 J. Escorihuela, R. Narducci, V. Compañ and F. Costantino, Proton Conductivity of Composite Polyelectrolyte Membranes with Metal–Organic Frameworks for Fuel Cell Applications, *Adv. Mater. Interfaces*, 2018, **6**, 1801146.
53 K.-D. Kreuer, A. Rabenau and W. Weppner, Vehicle Mechanism, A New Model for the Interpretation of the Conductivity of Fast Proton Conductors, *Angew. Chem., Int. Ed. Engl.*, 1982, **21**, 208–209.
54 N. Agmon, The Grotthuss mechanism, *Chem. Phys. Lett.*, 1995, **244**, 456–462.
55 M. Ekimova, C. Kleine, J. Ludwig, M. Ochmann, T. E. G. Agrenius, E. Kozari, D. Pines, E. Pines, N. Huse, P. Wernet, M. Odelius and E. T. J. Nibbering, From Local Covalent Bonding to Extended Electric Field Interactions in Proton Hydration, *Angew. Chem., Int. Ed.*, 2022, **61**, e202211066.
56 K.-D. Kreuer, Proton Conductivity: Materials and Applications, *Chem. Mater.*, 1996, **8**, 610–641.
57 T. Q. Nguyen and C. Breitkopf, Determination of Diffusion Coefficients Using Impedance Spectroscopy Data, *J. Electrochem. Soc.*, 2018, **165**, E826–E831.

58 Z. Xie, H. Wu, Q. Wu and L. Ai, Synthesis and performance of solid proton conductor molybdovanadosilicic acid, *RSC Adv.*, 2018, **8**, 13984–13988.
59 S. Haghighat, S. Ostresh and J. M. Dawlaty, Controlling Proton Conductivity with Light: A Scheme Based on Photoacid Doping of Materials, *J. Phys. Chem. B*, 2016, **120**, 1002–1007.
60 J. Fan, T. Wang, Y. Yuan, C.-L. Do-Thanh, X. Suo, Z. Yang, H. Chen and S. Dai, Mechanochemically Assisted Synthesis of High-Entropy Layer-Structured Dittmarite Analogues, *ACS Appl. Energy Mater.*, 2022, **5**, 3290–3297.
61 A. Amiri and R. Shahbazian-Yassar, Recent progress of high-entropy materials for energy storage and conversion, *J. Mater. Chem. A*, 2021, **9**, 782–823.
62 Y. Sun and S. Dai, High-entropy materials for catalysis: A new frontier, *Sci. Adv.*, 2021, **7**, eabg1600.
63 Y. Sone, P. Ekdunge and D. Simonsson, Proton Conductivity of Nafion 117 as Measured by a Four–Electrode AC Impedance Method, *J. Electrochem. Soc.*, 1996, **143**, 1254.
64 Y. Sun, Y. Yan, Y. Wang, Y. Li, J. Li and J. Yu, High proton conduction in a new alkali metal-templated open-framework aluminophosphate, *Chem. Commun.*, 2015, **51**, 9317–9319.
65 K. Scott, C. Xu and X. Wu, Intermediate temperature proton-conducting membrane electrolytes for fuel cells, *Wiley Interdiscip Rev Energy Environ*, 2014, **3**, 24–41.
66 W. H. J. Hogarth, S. S. Muir, A. K. Whittaker, J. C. Diniz da Costa, J. Drennan and G. Q. Lu, Proton conduction mechanism and the stability of sol–gel titanium phosphates, *Solid State Ionics*, 2007, **177**, 3389–3394.
67 P. G. M. Mileo, T. Kundu, R. Semino, V. Benoit, N. Steunou, P. L. Llewellyn, C. Serre, G. Maurin and S. Devautour-Vinot, Highly Efficient Proton Conduction in a Three-Dimensional Titanium Hydrogen Phosphate, *Chem. Mater.*, 2017, **29**, 7263–7271.
68 H.-R. Zhao, C. Xue, C.-P. Li, K.-M. Zhang, H.-B. Luo, S.-X. Liu and X.-M. Ren, A Two-Dimensional Inorganic–Organic Hybrid Solid of Manganese(II) Hydrogenophosphate Showing High Proton Conductivity at Room Temperature, *Inorg. Chem.*, 2016, **55**, 8971–8975.
69 K.-M. Zhang, Y.-L. Lou, F.-Y. He, H.-B. Duan, X.-Q. Huang, Y. Fan and H.-R. Zhao, The water-mediated proton conductivity of a 1D open framework inorganic-organic hybrid iron phosphate and its composite membranes, *Inorg. Chem. Commun.*, 2021, **134**, 109032.
70 M. Wang, H.-B. Luo, S.-X. Liu, Y. Zou, Z.-F. Tian, L. Li, J.-L. Liu and X.-M. Ren, Water assisted high proton conductance in a highly thermally stable and superior water-stable open-framework cobalt phosphate, *Dalton Trans.*, 2016, **45**, 19466–19472.
71 J.-W. Yu, H.-J. Yu, Q. Ren, J. Zhang, Y. Zou, H.-B. Luo, L. Wang and X.-M. Ren, Humidity-sensitive irreversible phase transformation of open-framework zinc phosphate and its water-assisted high proton conduction properties, *Dalton Trans.*, 2021, **50**, 8070–8075.
72 H.-X. Sun, H.-N. Wang, Y.-H. Zou and X. Meng, Tuning proton conduction by different particle sizes in open-framework metal phosphates, *Inorg. Chem. Commun.*, 2021, **124**, 108322.
73 S. Matsumura, R. H. Antisar, C. Lepiller, J. Gaudet, D. Guay, Z. Shi, S. Holdcroft and A. S. Hay, Ionomers for Proton Exchange Membrane Fuel Cells with Sulfonic Acid Groups on the End Groups: Novel Branched Poly(ether-ketone)s, *Macromolecules*, 2008, **41**, 281–284.
74 D. W. Lim and H. Kitagawa, Rational strategies for proton-conductive metal-organic frameworks, *Chem. Soc. Rev.*, 2021, **50**, 6349–6368.
75 J. Kim, S. Sengodan, S. Kim, O. Kwon, Y. Bu and G. Kim, Proton conducting oxides: A review of materials and applications for renewable energy conversion and storage, *Renewable Sustainable Energy Rev.*, 2019, **109**, 606–618.
76 R. Sigwadi, M. S. Dhlamini, T. Mokrani, F. Nemavhola, P. F. Nonjola and P. F. Msomi, The proton conductivity and mechanical properties of Nafion(R)/ZrP nanocomposite membrane, *Heliyon*, 2019, **5**, e02240.
77 A. Çalı, A. Şahin and İ. Ar, Experimental Investigation of boron phosphate Incorporated speek/pvdf blend membrane for proton exchange membrane fuel cells, *Int. J. Hydrogen Energy*, 2022, **47**, 40476–40490.
78 O. Zholobko, J. Hurley, X.-F. Wu, T. Aulich and J. Thakare, Intermediate-Temperature Proton Exchange Membranes Based on Cerium Ultraphosphate Composited with Polybenzimidazole, *J. Electrochem. Soc.*, 2022, **169**, 094505.